

Radar observations and a physical model of contact binary Asteroid 4486 Mithra

Marina Brozovic^{a,*}, Lance A.M. Benner^a, Christopher Magri^b, Steven J. Ostro^a, Daniel J. Scheeres^c, Jon D. Giorgini^a, Michael C. Nolan^d, Jean-Luc Margot^e, Raymond F. Jurgens^a, Randy Rose^a

^a Jet Propulsion Laboratory, California Institute of Technology, Pasadena, CA 91109-8099, USA

^b University of Maine at Farmington, Preble Hall, Farmington, ME 04938, USA

^c Aerospace Engineering Sciences, University of Colorado, Boulder, CO 80309-0429, USA

^d Arecibo Observatory, National Astronomy and Ionosphere Center, Arecibo, PR 00613, USA

^e Department of Earth and Space Sciences, University of California, Los Angeles, CA 90095-1567, USA

ARTICLE INFO

Article history:

Received 14 September 2009

Revised 3 January 2010

Accepted 31 January 2010

Available online 7 February 2010

Keywords:

Radar observations

Asteroids

ABSTRACT

Arecibo (2380 MHz, 12.6 cm) and Goldstone (8560 MHz, 3.5 cm) delay-Doppler radar images obtained in July and August of 2000 reveal that 4486 Mithra is an irregular, significantly bifurcated object, with a central valley ~380 m deep and a long axis potentially exceeding 2 km. With its bimodal appearance, Mithra is a strong candidate for a contact binary asteroid. Sequences of Goldstone images spanning up to 3 h per day show very little rotation and establish that Mithra is an unusually slow rotator. We used Goldstone and Arecibo data to estimate Mithra's 3D shape and spin state. We obtain prograde ($\lambda = 337^\circ$, $\beta = 19^\circ$) and retrograde ($\lambda = 154^\circ$, $\beta = -19^\circ$) models that give comparable fits, have very similar shapes roughly resembling an hourglass, and have a rotation period of 67.5 ± 6.0 h. The dimensions of these two models are very similar; for the prograde solution the maximum dimensions are $X = 2.35 \pm 0.15$ km, $Y = 1.65 \pm 0.10$ km, $Z = 1.44 \pm 0.10$ km. Dynamical analysis of our models suggests that in the past, Mithra most likely went through a period of even slower rotation with its obliquity close to 90° . The spin rate is predicted to be increasing due to thermal torque (YORP), while the obliquity, which is currently $+68^\circ$ and $+106^\circ$ for the prograde and retrograde models, respectively, is predicted to move away from 90° .

© 2010 Elsevier Inc. All rights reserved.

1. Introduction

4486 Mithra (1987 SB) was discovered on September 22, 1987 by E. Elst, V. Ivanova, and V. Shkodrov at the Bulgarian National Observatory in Smolyan. Mithra ($a = 2.20$ AU, $e = 0.66$, $i = 3.0^\circ$) belongs to the Apollo class and it crosses the orbits of both Earth and Mars. Its perihelion lies just outside the orbit of Venus, so it also makes close approaches (<0.02 AU) to this planet. Mithra has an absolute magnitude of 15.6, suggesting a diameter of roughly 2 km, but otherwise its physical properties are unknown. No light-curves have been reported and the taxonomic class is unknown. Here we report radar images and shape modeling of Mithra that reveal one of the most bifurcated and irregular shapes seen to date in the near-Earth population.

2. Observations and data reduction

Radar observations involve transmission of a circularly polarized signal and reception of echoes in the same and opposite circu-

lar polarizations (SC and OC). The duration of each transmit-receive cycle (or “run”) is determined by the target's distance. Each run can be analyzed as a sum of some number of statistically independent measurements or “looks” (Ostro, 1993; Magri et al., 2007). The data from different looks are combined in incoherent sums in order to reduce the fractional noise fluctuation by $\sqrt{N_{\text{looks}}}$.

We observed Mithra at Arecibo and Goldstone on eight dates during July and August 2000. Table 1 summarizes the radar observations. The subradar latitude (angular distance from the asteroid's equatorial plane to the radar line of sight) was changing from day to day as Mithra traversed $\sim 34^\circ$ on the sky from July 22 to August 9. At the time of the Arecibo observations, Mithra was still relatively distant (>0.18 AU) and we initially estimated that signal-to-noise ratios (SNRs) might be ~ 40 per day. However, the SNRs turned out to be much higher: several hundred per day. After July 30 Mithra moved too far south for Arecibo to track. Goldstone was able to observe Mithra at much closer distances as it moved south; our strongest images were obtained on August 9 when Mithra was within 0.07 AU and when the SNRs at Goldstone soared to more than a 1000 per day. After August 10 Mithra moved too far south for Goldstone to track. Closest approach was on August 14 at 0.0465 AU when Mithra was at a declination of -69° .

Fig. 1A shows continuous-wave (CW, Doppler-only) echo power spectra obtained at Arecibo (S-band, 2380 MHz) and Fig. 1B shows

* Corresponding author. Address: Mail Stop 301-121, Jet Propulsion Laboratory, California Institute of Technology, Pasadena, CA 91109-8099, USA. Fax: +1 818 393 7116.

E-mail address: marina.brozovic@jpl.nasa.gov (M. Brozovic).

Table 1

Radar observations of Mithra.

Date	Time range (UTC) START–STOP	Obs.	Type	Resolution		Runs	RA (°)	Declination (°)	Distance (AU)	Sol	Code
				(μs)	(Hz)						
July 22	17:41:33–18:27:26	A	CW	–	0.033	6	152	+6	0.245	13	–
	19:08:13–19:29:13	A	CW	–	0.033	3				13	–
July 23	17:47:46–17:51:34	A	CW	–	0.020	1	152	+6	0.233	15	–
	17:58:34–18:02:20	A	Ranging	4.0	–	1				15	4095
	18:24:09–18:27:55	A	Ranging	4.5	–	1				15	4095
July 25	17:32:41–17:36:08	A	CW	–	0.020	2	152	+4	0.212	17	–
	17:55:54–18:41:24	A	Imaging	0.500	0.030	7				17	65535
July 28	17:27:46–17:30:41	A	CW	–	0.020	1	152	+2	0.180	19	–
	17:36:15–18:48:57	A	Imaging	0.500	0.030	11				19	65535
August 06	18:49:47–19:18:02	G	CW	–	0.120	10	149	–14	0.091	24	–
	20:19:34–20:39:15	G	Ranging	10.0	–	7				26	255
	20:44:42–21:10:17	G	Ranging	11.0	–	9				26	255
	21:33:38–22:11:21	G	Imaging	0.250	0.065	13				26	255
August 07	22:48:08–23:59:19	G	Imaging	0.125	0.040	24				26	255
	18:14:18–20:32:27	G	Imaging	0.125	0.040	50	148	–17	0.083	26	255
	20:44:17–21:10:38	G	Imaging	0.125	0.040	10				26	255
August 08	18:04:52–19:44:59	G	Imaging	0.125	0.040	40	146	–22	0.074	26	255
	20:01:30–21:05:47	G	Imaging	0.125	0.040	26				26	255
August 09	21:21:16–21:26:53	G	Imaging	0.125	0.040	3	145	–27	0.067	26	255
	21:34:59–22:45:23	G	Imaging	0.125	0.040	11				26	255

Masterlog of Mithra radar observations. All observing dates refer to 2000. Arecibo and Goldstone observations were done monostatically with average transmitter powers of 900 kW at Arecibo and 430 kW at Goldstone. For the imaging data, the echoes were received in SC and OC polarizations at Arecibo and only in the OC polarization at Goldstone. Arecibo observations were in S-band (2380 MHz, 12.6 cm) and Goldstone observations were in X-band (8560 MHz, 3.5 cm). The time range shows the start and end of reception of echoes on each day. The data resolution is given in time delay (μs) and Doppler frequency (Hz). Right ascension, declination, and distance in AU are given at the beginning of each observation session. We also list the number of transmit–receive cycles (runs) and the orbital solution (sol) used to compute delay–Doppler ephemeris predictions. Code refers to the length of the repeating binary phase code.

a single Goldstone CW spectrum (X-band, 8560 MHz) from August 6. Mithra's OC echoes are obviously stronger than its SC echoes, although the Goldstone SC spectrum appears stronger than we would expect based on the Arecibo data if scattering properties at 3.5 cm and 12.6 cm were identical. This may indicate higher surface roughness on 3.5 cm scales compared to 12.6 cm scales. Mithra's bandwidths are very narrow, ~ 0.2 Hz at Arecibo and ~ 0.8 Hz at Goldstone, suggesting a very slow rotation (period of days) and/or close to a pole-on view of the object. The statistically significant dip in the center of the OC spectrum on July 22 (and possibly July 25) is evidence for a central concavity. The SC/OC ratio in the center of the spectrum is higher because of a double-reflection backscatter from two almost perpendicular surfaces at the center of the object. Similar evidence for a central concavity was observed in CW spectra of Asteroids 4769 Castalia (Ostro et al., 1990), 3908 Nyx (Benner et al., 2002), and 2063 Bacchus (Benner et al., 1999).

Fig. 2 shows representative delay–Doppler images of Mithra from each day. Goldstone delay–Doppler images achieved resolution in range as fine as 0.125 μs (19 m) and we were able to place hundreds of pixels on the object. Table 2 lists the bandwidths and visible extents obtained by visual inspection of the delay–Doppler images where we counted the pixels that we subjectively deemed above the noise level. If Mithra were a sphere, we would see only about half of the object, so in general, we try to estimate the true extents by doubling the visible extents. We initially consider the long axis to be between 1.5 km and 2.5 km. For reasons that will become clear shortly, we are confident that Mithra's subradar latitude was at least several tens of degrees from the equator during our observations.

Mithra looks like a double-lobed object. The valley between the lobes is ~ 380 m deep based on the August 8 images. Images from July 25 and 28 and August 7 and 8 also reveal a short “bridge” between the lobes which makes us confident that the lobes are in contact. Images from August 6 contain a radar dark feature (“Feature 1”) near the leading edge of the bottom lobe. We suspect it is a concavity. “Feature 2” marks a radar bright area near the leading edge

of the right lobe on August 8. This could be interpreted as something resembling a “knuckle”. We observe a radar dark formation similar to “Feature 1” on the leading edge of the top lobe on August 9 image (“Feature 3”). This could be another concavity. The lobes show sharp drop-offs on the sides of the echo on August 7 and 8, suggesting flat sides that are almost parallel to the line of sight.

The echo bandwidths (Table 2) are consistently narrow and suggest slow rotation, a nearly pole-on view, or both. The bandwidth decreased between July 22 and August 6, when it reached a minimum, remained very narrow on August 7, and then noticeably increased between August 7 and 9. Additional evidence for the change in the subradar latitude is the increase in the distance between the leading edges of the lobes on August 6 (~ 260 m) and August 9 (~ 500 m). This suggests that the subradar point moved toward the equator after August 7.

The Doppler broadening is given by $B = 4\pi D \cos(\delta)/(\lambda P)$, where B is the bandwidth, D is the object's dimension in the plane of the sky perpendicular to the spin vector, λ is radar wavelength, P is the period of rotation, and δ is the subradar latitude. We used this equation to constrain Mithra's period. Due to the irregular shape, individual extents and bandwidths will produce a wide range of rotation periods. The upper bound on Mithra's period is established by assuming $\delta = 0^\circ$ (equatorial view). The bandwidths consistently imply a period up to several days.

We also investigated whether Mithra's rotation can be detected directly in the images. Fig. 3 shows two delay–Doppler images from August 8. These images have mean times 2.63 h apart. Drawing white parallel lines as a reference highlights the slow rotation. The receding edge moved about $6(\pm 1)$ rows, each 19 m in range or ~ 95 –133 m. Let us assume that the arc of the rotation is small enough during 2.63 h so that the length of the arc is roughly equal to this distance. This gives a tangential velocity of 0.012 – 0.014 m s $^{-1}$. Based on the dimensions from Table 2 and on the depth of the valley between the lobes, we estimate the distance of the leading edge from the center-of-mass to be ~ 500 – 700 m. This gives an angular velocity of 4 deg h $^{-1}$ to 6 deg h $^{-1}$ and a rotation period in the realm of 60–90 h.

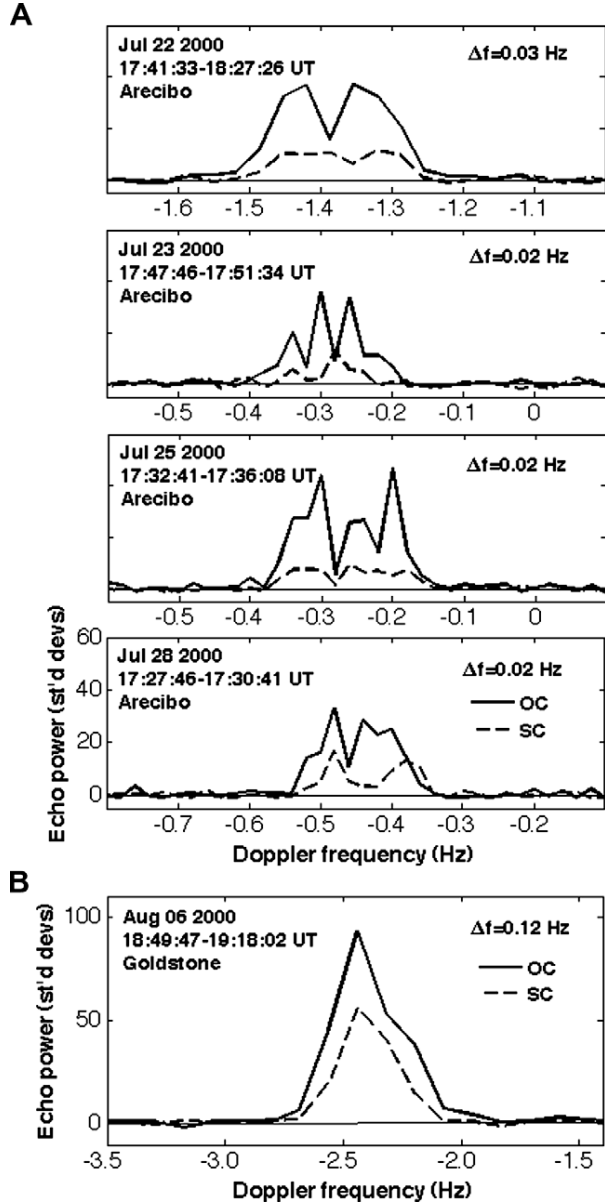


Fig. 1. (A) Mithra OC and SC echo power spectra obtained at Arecibo. Each spectrum is a weighted sum of the number of runs from each day given in Table 1. The number of looks for each day is 48, 3, 8 and 4, respectively. Δf is the Doppler frequency resolution. (B) OC and SC spectra obtained at Goldstone. The number of looks is 77.

3. Shape modeling

We used the *Shape* software to estimate Mithra's 3D shape and spin state. *Shape* uses constrained, weighted least squares and the input data may be delay-Doppler images, CW spectra, optical light-curves, and/or plane-of-sky images. The software was originally written by Hudson (1993) and pioneered on 4769 Castalia (Hudson and Ostro, 1994), 4179 Toutatis (Hudson and Ostro, 1995), and 1620 Geographos (Hudson and Ostro, 1999). There have been many recent improvements (Magri et al., 2007) and the software continues to expand and acquire new capabilities. The parameter space is very large and the user needs to constrain this space by the set of initial values, step sizes, and convergence criteria. We went through iterative adjustments of the input delay-Doppler



Fig. 2. Selected delay-Doppler images of Mithra from each day. Time delay increases from top to bottom and Doppler frequency increases from left to right. Arecibo images were scaled in Doppler by the ratio of observing frequencies to enable direct comparison with Goldstone images. The resolution for Arecibo data is $0.5 \mu s \times 0.03$ Hz and $0.125 \mu s \times 0.04$ Hz for Goldstone data. If we convert time delay into distance, the vertical dimension of each image is 1350 m. Arrows indicate features discussed in the text. Other images obtained on each day look very similar.

and CW data weights in order get the optimal fits both visually and in terms of χ^2 goodness of fit.

3.1. Shape modeling of Mithra

The first stage of shape modeling is to fit an ellipsoid. Mithra's bifurcated shape forced us to use a two-component model in the early stages of the modeling. The initial model consisted of a pair of identical ellipsoids. Each ellipsoid was parameterized with its

Table 2

Bandwidths and visible extents in delay-Doppler images.

Date	Obs	Left/top bandwidth (Hz)	Right/bottom bandwidth (Hz)	Total S-band bandwidth (Hz)	Total X-band bandwidth (Hz)	Visible range (m)
July 25	A	0.15	0.09	0.24 ± 0.03	0.86 ± 0.11	675 ± 75
July 28	A	0.12	0.09	0.21 ± 0.03	0.76 ± 0.11	750 ± 75
August 06	G	0.32	0.32		0.32 ± 0.04	638 ± 40
August 07	G	0.28	0.32		0.60 ± 0.04	544 ± 40
August 08	G	0.36	0.52		0.88 ± 0.04	600 ± 40
August 09	G	0.80	0.52		1.02 ± 0.04	1070 ± 40

Doppler bandwidths and visible extents of Mithra estimated by visual inspection from delay-Doppler images with resolutions given in Table 1. We assign uncertainties based on the data resolution and our subjective estimate of how precisely we are able to determine Mithra's dimensions. We label components "left/top" or "right/bottom" based only on their location in the delay-Doppler imaging. Doppler bandwidth of each component is given in S-band (2380 MHz) for Arecibo (A) and X-band (8560 MHz) for Goldstone (G). Total bandwidth does not necessarily equal the sum of the component bandwidths due to echo overlap in the images. In order to facilitate direct bandwidth comparison between Arecibo and Goldstone data, Mithra's total bandwidths (July 25 and 28) have been multiplied by 3.6 to convert from S-band to X-band.

three principal axis dimensions and three offsets in the x , y , and z directions from the center-of-mass. At this point, we tested a wide range of long axis lengths (1.5 km, 1.8 km, 2.2 km and 2.5 km). Our goal was to establish which size reproduces the visible extent as observed in the images (Fig. 2). In *Shape*, an ellipsoid is constructed from triangular facets and the size of the facets controls the modeling resolution. This becomes particularly important in the later stages of modeling.

Modeling the lobes as two spheroids was useful only for the very early stages of the fit while we were trying to constrain the large parameter space. In the second stage of the modeling, the shape was converted into a single component model by using a 10th order spherical harmonic series. In the third and final stage of modeling, we converted the 10th order harmonic series model into a model that consisted of 3000 vertices defining 5996 triangular facets. The approximate angular resolution is 4°. The parameter space was well constrained at this time, and the vertex fit was used to further refine Mithra's shape and other physical parameters.

Shape also estimates the radar scattering law, the spin state, the radar calibration, as well as the corrections to the delay-Doppler prediction ephemerides. We used a simple cosine law to model the radar reflectivity of the surface:

$$\frac{d\sigma}{dA} = R(C + 1)(\cos \alpha)^{2C} \quad (1)$$

Here, σ is a radar cross-section, A is the target surface area, α is the scattering angle, R is the Fresnel reflectivity and C is a measure of the specularity of the scattering (Michel et al., 1996).

3.2. Mithra's spin state

Our initial modeling assumption was that Mithra rotates about its short principal axis (PA rotation). *Shape* uses four parameters that define a principal axis spin state: the pole's ecliptic longitude

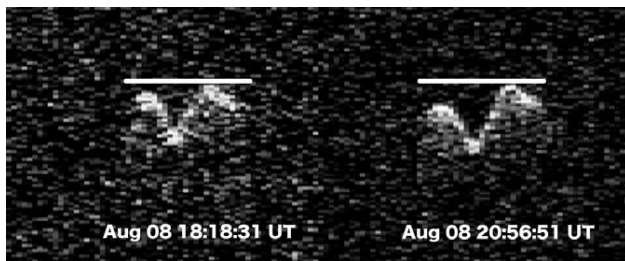


Fig. 3. Delay-Doppler images from August 8, separated by 2.63 h, demonstrate that Mithra is a very slow rotator. The images show counterclockwise rotation where the receding edge has moved $\sim 6 \pm 1$ rows (each 19 m long) relative to the horizontal white line. Delay-Doppler images are north–south ambiguous so the counterclockwise rotation does not distinguish between prograde and retrograde rotation.

λ , latitude β , rotation phase ψ at an arbitrarily chosen reference epoch, and the rotation period P about the short principal axis.

Initially, we used *Shape* to conduct a grid search for the pole direction and the rotation period. We limited our search to the prograde model (the retrograde model will be discussed in the following section). The pole directions were initialized in 20° intervals from 0° to 360° in λ and in 15° intervals from 0° to 90° in β . The periods were first investigated in 10-h increments from 50 h to 90 h. *Shape* was allowed to adjust the pole direction and period in each of the grid search runs. This was a very labor-intensive approach, with many subjective estimates of which pole-period combinations appear to work best. The χ^2 goodness of fit is not very useful at the ellipsoid stage of the modeling because Mithra has such an irregular shape. We found that a visual inspection of the fits is a much better way to pinpoint candidate models. We were mainly interested in reproducing the bandwidths and orientation of the two lobes (approximated as the ellipsoids), which we used as a starting point for the harmonic stage of fitting.

Later in the analysis, we investigated a more straightforward method to estimate the pole direction based purely on the predicted variation in subradar latitude during our observations. We investigated poles that provide a subradar latitude above 50° from the equator (either north or south) on August 6 and 7, with a subradar latitude roughly constant or increasing between July 22 and August 7, and then decreasing after August 7 (see Fig. 2). The requirement that the subradar latitude on August 6 and 7 has to be above 50° comes from considering a suite of plausible diameters between 1.5 and 2.5 km and rotation periods between 60 and 150 h and adjusting δ to match the observed range of bandwidths. At this point we made no selection based on the amount of subradar latitude change. This very general selection eliminated the majority of the candidate poles and we were left with the pole regions highlighted in Fig. 4. After this we narrowed down our estimates of Mithra's size and rotation period by using *Shape* to run the forward problem for a series of hand-edited models spanning a range of periods and ellipsoid sizes. In order to reproduce the longest visible extent observed on August 9, the high subradar latitudes pushed Mithra's longest axis to be in the realm of 2.2–2.5 km. The rotation period was more difficult to pinpoint because at high subradar latitudes, the bandwidth changes substantially for a slightly different pole direction. Our conclusion is that the bandwidth is much more sensitive to the change in pole direction than the change in period. Our preliminary period estimate based on the ellipsoidal stage of the fit was between 60 and 75 h.

We continued to refine Mithra's shape and spin state through a one component harmonic fit and finally through a vertex fit. The vertex mode approximated Mithra's shape with 5996 triangular facets. The final pole direction in ecliptic coordinates is $\lambda = 337^\circ$, $\beta = 19^\circ$ (Fig. 4 shows our estimate and their associated errors). The best rotation period estimate for Mithra is 67.5 ± 6.0 h. The uncertainty limits include Mithra's alternative periods, also ob-

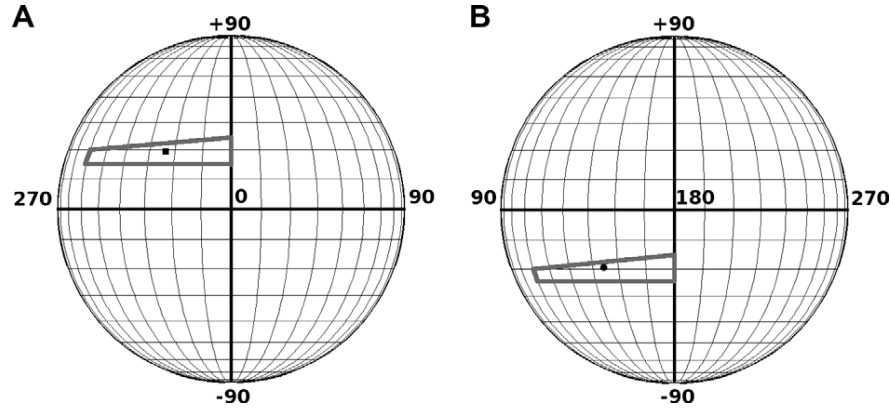


Fig. 4. 3- σ region for viable pole solutions. (A) Prograde pole (black square) is contained inside an uncertainty polygon with pole boundaries (λ, β) at $(0^\circ, +15^\circ)$, $(0^\circ, +25^\circ)$, $(300^\circ, +20^\circ)$ and $(300^\circ, +15^\circ)$. (B) Retrograde pole (black circle) is contained inside 3- σ region of $(180^\circ, -15^\circ)$, $(180^\circ, -25^\circ)$, $(120^\circ, -20^\circ)$ and $(120^\circ, -15^\circ)$.

tained during the vertex stage of modeling, of 61.9 h and 71.9 h; these two models have poorer χ^2 values than our preferred model, but visually the fits are close enough that these periods cannot be excluded. This is partly due to the fact that our data covered fewer than seven rotations and we sampled only a limited number of orientations with respect to the line of sight.

3.3. “Mirror” model of Mithra

The viewing geometry never changed enough to distinguish between prograde and retrograde rotation. Here, we define retro-

grade rotation as right-hand rotation about the pole with an obliquity greater than 90° . Multiple apparitions at different sky positions, more dates with radar observations, longer tracks across the sky during a single apparition, and possibly photometry would provide enough geometric leverage to resolve the ambiguity. The issue of the so-called “mirror” models has been discussed previously in Hudson et al. (1997) and Hudson and Ostro (1999). In summary, we construct a mirror model by swapping the position of the triangular facets about the y - z plane (a left-right reflection in the plane defined by the short and intermediate principal axes) and by reversing the sense of rotation ($P \rightarrow -P$) and phase

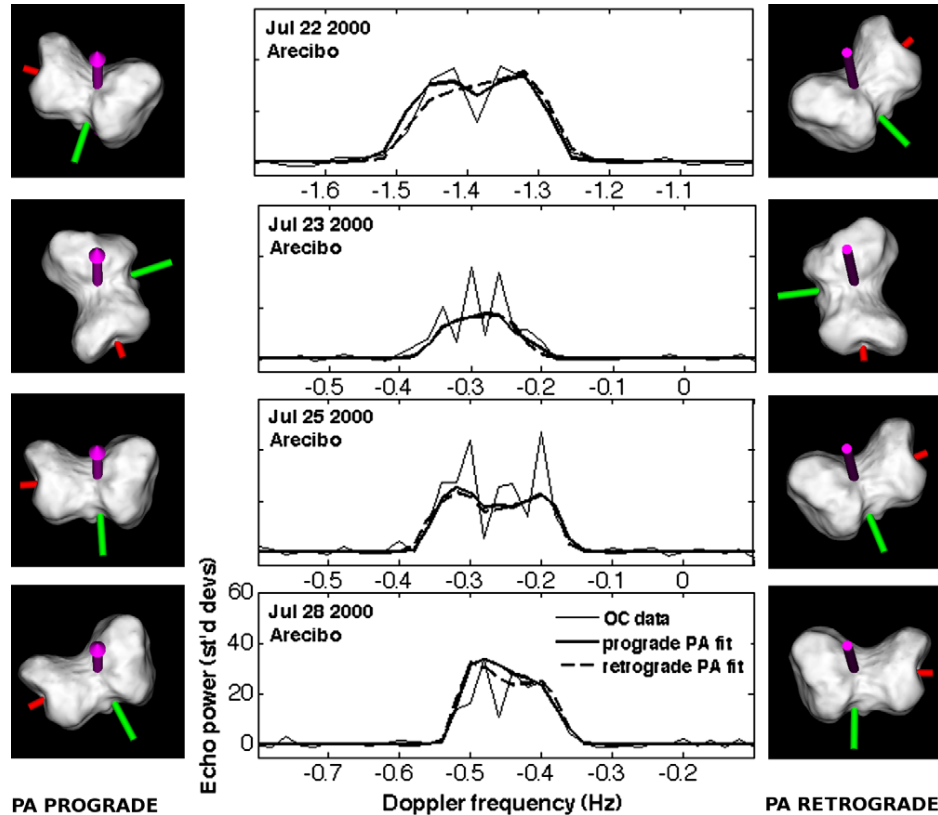


Fig. 5. Arecibo OC echo power spectra, prograde fits, and retrograde fits for each radar track. The spectral resolution is 0.03 Hz on the first date and 0.02 Hz on the other dates. The number of looks on each day is 48, 3, 8, and 4, respectively. The side panels show plane-of-sky renderings of the models. The magenta arrow shows the orientation of the spin vector, and the red and green shafts denote the positive ends of the long and the intermediate principal axes. (For interpretation of the references to color in this figure legend, the reader is referred to the web version of this article.)

($\psi \rightarrow -\psi$). This mirror model gives the same radar echo as the initial model. After the initial inversion, we let *Shape* further adjust all the vertices and spin state parameters. Our mirror model closely resembles the original model of Mithra due to the geometric constraints of the nearly pole-on view in the radar data.

The mirror pole direction is $\lambda = 154^\circ$ and $\beta = -19^\circ$, which is 177° from the other pole (also shown in Fig. 4). For the prograde pole, the subradar latitude increased from 75° to 79° from July 22 to 28, reached a maximum of 83° on August 6, and decreased to 69° by August 9. For the retrograde model, a virtually identical sequence occurs, but with southern subradar latitudes.

3.4. Shape modeling fit to the data

Fig. 5 shows OC CW data, fits, and plane-of-sky (POS) views of the prograde and retrograde models. A primary objective was to obtain the correct bandwidth on each of the observing days, since this is closely correlated with our spin state estimate. Overall, the modeled CW spectra match the bandwidths and the basic structure

of the data reasonably well. We used the simple cosine law in Eq. (1) to model the radar scattering, which limits how well the details (e.g. the depth of the bifurcation) may be matched. Due to the number of looks ($N = 48$) in the spectrum on July 22, the central dip is statistically significant. The number of looks in the other spectra is less than 10, which means that the echoes are dominated by self-noise and precise fits to the dips and peaks would be “fitting the noise”.

Fig. 6 shows delay-Doppler images, fits and POS views for the prograde and retrograde models. We included the complete imaging dataset (Table 3) in the modeling, but because of Mithra’s slow rotation, all of the images from each day look very similar, so to save space we show only one image per day. Overall, our model reproduces the orientation, visible extent, and large-scale attributes observed in the delay-Doppler images. Nevertheless, there are features that we do not fit as well as we would like. It is worth noting that within the 3σ uncertainty pole region marked in Fig. 4, two poles that are only a few degrees away from each other will reach slightly different (high) subradar latitudes. Since $B \sim \cos(\delta)$,

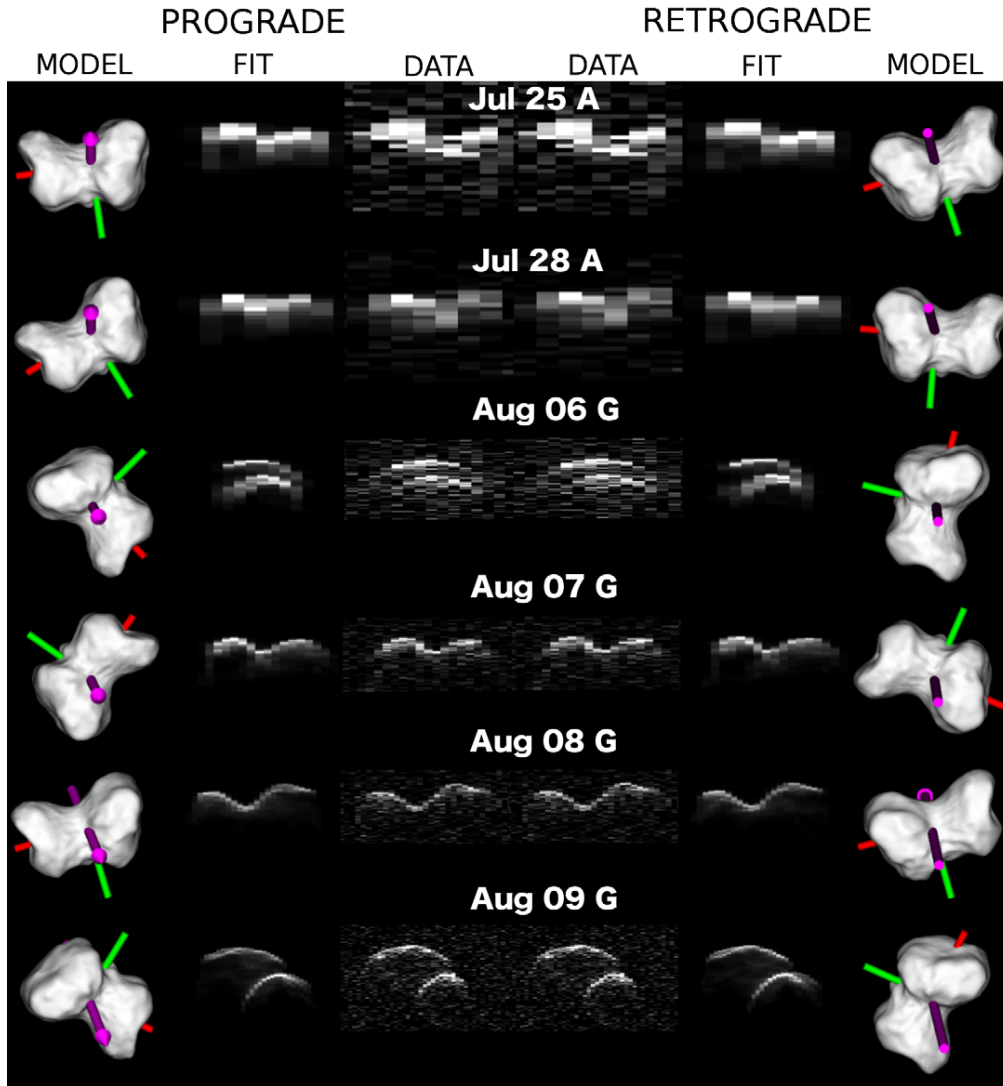


Fig. 6. Collage of delay-Doppler radar images, fits, and plane-of-sky renderings of the models. The data are grouped by day and observatory (“A” = Arecibo, “G” = Goldstone). The format for each row is, from left to right: prograde model plane-of-sky view, prograde fit, observed delay-Doppler image at the scale of the prograde fit, observed delay-Doppler image at the scale of the retrograde fit, retrograde fit, retrograde model plane-of-sky view. In the data and fits, time delay increases from top to bottom, and Doppler frequency increases from left to right. The data and the fits frames have dimensions of $20 \mu\text{s}$ in time delay (3.0 km in range) and 0.25 Hz , 0.24 Hz , 0.86 Hz , 0.82 Hz , 1.35 Hz and 1.56 Hz in Doppler frequency from first to the last date. The plane-of-sky view is contained in a $3.0 \times 3.0 \text{ km}$ square with 301×301 pixels.

Table 3

Delay-Doppler imaging dataset used in Shape modeling.

Date	Time range (UTC) START–STOP	Obs.	Resolution		Looks	Runs	Phase pro/retro	
			(μ s)	(Hz)			($^{\circ}$)	($^{\circ}$)
July 25	18:02:55–18:48:25	A	0.5	0.030	42	7	277	274
July 28	17:42:14–18:43:00	A	0.5	0.030	48	10	301	250
August 06	21:34:10–21:49:58	G	0.25	0.065	24	6	184	350
	21:52:09–22:11:21		0.25	0.065	28	7	186	349
	22:48:59–23:10:47		0.125	0.040	16	8	191	343
	23:13:11–23:34:59		0.125	0.040	16	8	193	341
	23:37:27–23:59:11		0.125	0.040	16	8	195	339
August 07	18:15:09–18:35:04	G	0.125	0.040	16	8	299	237
	18:37:21–18:57:13		0.125	0.040	16	8	301	235
	18:59:29–19:19:28		0.125	0.040	16	8	303	233
	19:21:45–19:41:50		0.125	0.040	16	8	306	231
	19:44:08–20:03:59		0.125	0.040	16	8	308	229
	20:06:22–20:32:27		0.125	0.040	20	10	310	226
	20:45:11–21:10:38		0.125	0.040	20	10	313	223
August 08	18:13:20–18:23:42	G	0.125	0.040	5	5	70	108
	18:25:58–18:44:07		0.125	0.040	8	8	72	107
	18:46:16–19:04:15		0.125	0.040	8	8	74	105
	19:06:31–19:24:23		0.125	0.040	8	8	75	103
	19:27:37–19:44:59		0.125	0.040	8	8	77	101
	20:02:21–20:22:41		0.125	0.040	9	9	81	98
	20:24:56–20:45:45		0.125	0.040	9	9	83	96
	20:47:54–21:05:47		0.125	0.040	9	9	85	94
August 09	21:35:52–21:54:34	G	0.125	0.040	9	9	219	321
	21:56:41–22:15:17		0.125	0.040	9	9	221	319
	22:22:03–22:45:23		0.125	0.040	11	11	223	316

Imaging data used in *Shape* modeling. Times indicate the start and end of the data that are used in each delay-Doppler image. We list the image resolution, number of looks and run number(s), as well as the phase of the rotation in the middle of the time interval based on the prograde and retrograde models. Delay-Doppler images from Fig. 6 are marked in bold. Only OC data were used for modeling.

and since $\cos(\delta)$ varies rapidly near the poles, this difference in subradar latitude can easily create a bandwidth mismatch of tens of percent. There is a modest bandwidth mismatch on August 6, where the fits (both prograde and retrograde) appear one Doppler bin ($\sim 12\%$) narrower than in the data. Conversely, the images are noisy enough that it is difficult to make a strong statement on the bandwidth mismatch where the fits are slightly wider than the observations. There is also a three-Doppler bin ($\sim 19\%$) bandwidth mismatch on the trailing lobe in the August 9 delay-Doppler images. We have increased the weights on these images up to 250 times with respect to the rest of the dataset in an attempt to bring out the corresponding shape features, but we never achieved better bandwidth match on the trailing lobe. This could be due to the fact that the leading lobe is wider in bandwidth and has a stronger echo, so it dominates χ^2 on this date. This is similar to the situation that was encountered with models of 25143 Itokawa, when the images showed a narrower leading edge at some orientations that was never reproduced to a satisfactory degree in the models (Ostro et al., 2004, 2005).

3.5. Mithra's size and shape

Fig. 7A and B shows principal axis views of the prograde and retrograde models. Mithra consists of two irregular lobes that are connected by a short bridge or a neck. The shape is elongated; the prograde model has dimensions of $2.35 \times 1.65 \times 1.44$ km and the retrograde model has dimensions $2.48 \times 1.70 \times 1.48$ km. Mithra has a moderate elongation with $X/Y \approx 1.42 \pm 0.15$ for the prograde model and $X/Y \approx 1.46 \pm 0.15$ for the retrograde model, values slightly lower than the average NEA elongation as derived from radar shape estimations (http://echo.jpl.nasa.gov/~lance/nea_elongations.html); 1.55 ± 0.47 ($N = 28$). Table 4 summarizes the physical properties of Mithra from the prograde and retrograde models. The uncertainties on the dimensions are inclusive of both

prograde and retrograde models. This is a more conservative number than the values that we have obtained based on the statistical variations among modeling runs.

The radar coverage is limited to less than 50% of Mithra's surface, and is centered at high latitudes, so the shape on the hemisphere unseen by the radar is not well constrained. The shape on that side is constrained dynamically, since we assumed that Mithra is a uniform density object that rotates about its short principal axis – that is, we employed penalty functions that forced the model's overall shape to conform to these two requirements. However, it is unlikely that this particular shape of the unseen side is the only possible solution. Penalties that controlled concavities and smoothness also affect the shape on the hidden hemisphere, and in the absence of data, this hemisphere has a much less pronounced bimodal appearance because the central concavity has been smoothed out.

3.6. Non-principal axis rotation?

Is Mithra a non-principal axis (NPA) rotator? Preliminary inspection of the images (Ostro et al., 2000) hinted that Mithra could be an NPA rotator. We have investigated this possibility extensively. We find that the delay-Doppler images and CW spectra are consistent with short axis mode NPA rotation that is very close to PA rotation, but that NPA rotation is not required to obtain good fits to the data (see [supplementary material](#)). Thus, we adopt a conservative approach in which we favor PA rotation. However, we include the NPA rotation state in our estimate of the spin vector ω by using ω_x and ω_y components as the uncertainty limits of the PA state (Table 3).

3.7. Optical albedo

Our shape model allows us to estimate Mithra's visual geometric albedo, which we calculated from $p_v = (1329/D)^2 \times 10^{-0.4H_v}$

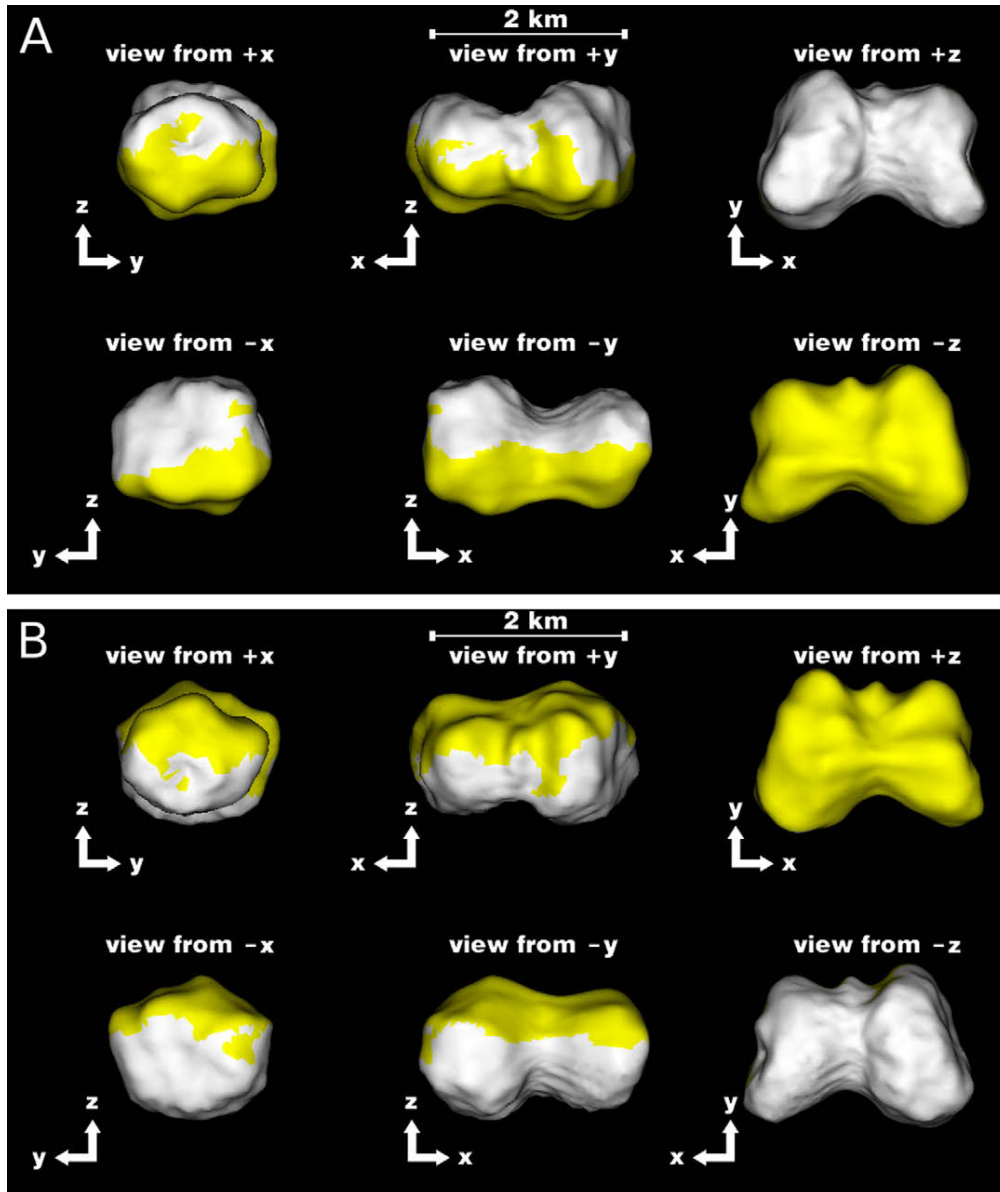


Fig. 7. Principal-axis views of the Mithra shape models. Both models have 3000 vertices that form 5996 triangular facets with 4° spacing between the adjacent vertices. Yellow shading indicates areas that are not well constrained by the data because the radar scattering angle was always greater than 60° . (A) Prograde model with dimensions of $2.35 \times 1.65 \times 1.44$ km. (B) Retrograde model with dimensions of $2.48 \times 1.70 \times 1.48$ km.

(Campins et al., 1985; Pravec and Harris, 2007). For an absolute visual magnitude of $H_v = 15.6$ and the equivalent diameter of the prograde model, $D = 1.69$ km, we obtain $p_v = 0.36$. The optical albedo calculated for the slightly larger ($D = 1.75$ km) retrograde model is 0.33. Both results imply that Mithra is optically bright and that its albedo is consistent with an S-class object.

4. Mithra orbit refinement

Radar astrometric data are referenced to the center-of-mass location of an asteroid's echo at the time of the observations. The observer usually estimates this location (and its uncertainty) visually in time delay and Doppler frequency. One advantage of having a 3D model is that, with the assumption of homogeneous density, *Shape* gives precise locations of the center of mass and enables us to assign much smaller uncertainties than we previously estimated by eye and thus significantly improves the orbit.

Table 5 lists model-based astrometric measurements and post-fit residuals from the new orbital solution (#68). We used center-of-mass estimates obtained from the prograde model, although the other model gave virtually identical values. The small size of the post-fit residuals in Table 5 is an indicator of the consistency between the shape model's center of mass and optical astrometry spanning 22 years of measurement. The dynamical model of the solution includes the relativistic point-mass gravitational perturbations of the Sun, Moon, Planets, Ceres, Pallas, and Vesta, in a coordinate system defined by the DE405 planetary ephemeris solution, a quasar-based frame generally within 0.01 arcsec of the optical FK5/J2000 frame.

Table 6 lists orbital elements for the latest solution, and Table 7 lists past and present encounters by Mithra with various bodies in the Solar System. The encounter observed in 2000 was the closest with Earth for the foreseeable future. Mithra has frequent encounters with Venus at distances closer than with Earth.

Table 4

Physical properties of Mithra models.

	Prograde model	Retrograde model
Pole direction (°)	$\lambda = 337_{-37}^{+23}, \beta = 19_{-4}^{+6}$	$\lambda = 154_{-34}^{+26}, \beta = -19_{-6}^{+4}$
Principal axis		
X	2.35 ± 0.15 km	2.48 ± 0.15 km
Y	1.65 ± 0.10 km	1.70 ± 0.10 km
Z	1.44 ± 0.10 km	1.48 ± 0.10 km
Axis ratios		
X/Y	1.42 ± 0.15	1.46 ± 0.15
Y/Z	1.15 ± 0.15	1.15 ± 0.15
Equivalent diameter	1.69 ± 0.05 km	1.75 ± 0.05 km
Surface area	11.08 ± 1.00 km ²	11.85 ± 1.00 km ²
Volume	2.53 ± 0.30 km ³	2.79 ± 0.30 km ³
DEEVE		
X	2.56 ± 0.15 km	2.66 ± 0.15 km
Y	1.51 ± 0.10 km	1.55 ± 0.10 km
Z	1.25 ± 0.10 km	1.29 ± 0.10 km
Spin vector rates		
ω_x	$0.0_{-12.0}^{+0.0}$ deg day ⁻¹	$0.0_{-0.0}^{+12.0}$ deg day ⁻¹
ω_y	$0.0_{-7.0}^{+4.0}$ deg day ⁻¹	$0.0_{-4.0}^{+7.0}$ deg day ⁻¹
ω_z	128.1 ± 10.00 deg day ⁻¹	127.8 ± 10.0 deg day ⁻¹
Rotation period	67.5 ± 6.0 h	67.6 ± 6.0 h
Radar scattering law		
R	0.11 ± 0.04	0.10 ± 0.04
C	0.81 ± 0.10	0.90 ± 0.10
Optical albedo	$p_v = 0.36 \pm 0.03$	$p_v = 0.33 \pm 0.03$

Pole direction is given in the ecliptic reference frame. Uncertainties in the physical dimensions and other properties were determined based on statistical variations between various modeling runs. “DEEVE” stands for dynamically equivalent, equal volume ellipsoid. We also list the cosine radar scattering law parameters R and C.

5. Disk-integrated properties

Table 8 lists disk-integrated properties for Mithra. We combined the circular polarization ratios (SC/OC) from both Arecibo data and previously reported Goldstone measurements (Benner et al., 2008) and obtained an average of 0.31 ± 0.14 . The Arecibo data show significant internal scatter. This could be due to differences in the surface properties (e.g. a heterogeneous regolith distribution), which is possible, but somewhat speculative, or due to calibration issues that varied from day to day, which is perhaps the more likely explanation. An additional puzzle is that the single Goldstone SC/OC measurement from August 6 is 23% larger than the highest measured SC/OC ratio from Arecibo. Although the cause of the difference is most likely in the calibration of the two systems, it is also possible that the different ratios represent wavelength-dependent properties of Mithra's surface.

Table 5

Radar astrometry estimated from Shape modeling.

UTC epoch of the echo reception	Obs.	Time delay estimate (s)	Std. (μs)	Residual (μs)	Doppler frequency estimate (Hz)	Std. (Hz)	Residual (Hz)
2000 07 25 18:24:00	A	209.75319776	±1.5	0.044	298051.847	±0.060	0.017
2000 07 28 18:11:00	A	177.91994343	±1.5	−0.227	288133.959	±0.060	0.012
2000 08 06 21:40:00	G	88.19926323	±0.5	−0.224	852224.564	±0.150	0.050
2000 08 07 18:20:00	G	81.29776526	±0.5	−0.196	843188.813	±0.150	0.040
2000 08 08 18:20:00	G	73.14822281	±0.5	−0.002	790636.399	±0.150	−0.029
2000 08 09 21:40:00	G	64.61227690	±0.5	−0.056	692491.562	±0.150	0.084

Mithra Shape model estimates of the positions of the center of mass in round-trip time delay and Doppler frequency at the listed time epoch at the telescope reference point. The measurement reference point for Arecibo is the center of curvature of the telescope's main reflector. For Goldstone, it is the intersection of the elevation and azimuthal axes of the 70-m antenna (DSS-14). The uncertainties (Std.) in time delay and Doppler frequency are assigned based on the data resolution. Post-fit observed–computed residuals are the remaining difference between the measurement and the orbit solution best-fitting (in a least-squares sense) the current combined optical and radar measurement dataset (JPL solution #68).

Table 6

Mithra orbital solution #68.

J2000 heliocentric IAU76 ecliptic coordinates Epoch JD 2454831.50000 = 2008 December 31.0 CT (coordinate time)		
Osculating element	Value	Std. dev. (σ)
Eccentricity	0.6605381599922822	±0.0000000268
Perihelion distance	0.7482044535752296	±0.0000000595 AU
Time of perihelion	2455311.4614267998 (2010 April 24.96143)	±0.0000587801 d (JDCT)
Longitude of ascending node	82.32254982266609	±0.0001987216°
Argument of perihelion	168.82513600854736	±0.0001935271°
Inclination	3.03429004980261	±0.0000062067°
Semi-major axis	2.204090019538628	±0.0000000237 AU
Orbital period	1195.205048431684 (3.27223574571639 year)	±0.00001930 d
Mean anomaly	215.43391581666017	±0.0000020254°

Mithra orbit solution #68 which was estimated from 310 optical measurements, reported over the time span January 29, 1987 to December 20, 2008, and 12 delay-Doppler measurements derived from the shape model, as listed in Table 5. The data types were fit simultaneously within their assigned measurement uncertainties. The less precise delay-Doppler measurements that were made at the time of the observations, using visual inspection of the data rather than a shape model, were excluded. The post-fit residual mean (RA, DEC) for the optical data is $(-0.049 \pm 0.61, 0.071 \pm 0.60)$ arcsec. Its respective normalized rms (root reduced chi-square) is 0.448. The delay mean residual is -0.11 ± 0.12 μs, with a normalized residual delay rms of 0.255 μs. The Doppler mean residual is 0.029 ± 0.038 Hz with a normalized residual rms of 0.330 Hz. The combined radar-plus-optical normalized residual rms is 0.445.

The SC/OC ratio provides a measure of the near-surface roughness. Ratios that are small (up to ~ 0.2) indicate smoothness at the radar wavelengths (centimeter to decimeter scales) while ratios higher than 0.5 indicate significant surface and near-surface roughness. Recently, Benner et al. (2008) found that there is a strong correlation between the SC/OC ratio and visible-infrared taxonomic class. The mean SC/OC in the sample of 214 NEAs is 0.34 ± 0.25 . The means for different classes ranged from SC/OC < 0.2 (M, P, D and F) through $0.2 \leq \text{SC/OC} < 0.5$ (S, C and O) to SC/OC > 0.5 (V, E and X). We conclude that Mithra's SC/OC ratio does not tie the object to a specific taxonomic class, although the class could be S (consistent with our optical albedo estimate). The C class and perhaps P class is also consistent with the SC/OC ratio, although their optical albedos are much darker than our estimates for Mithra. Our results probably exclude the M, E, and V classes because their SC/OC ratios are either too low or too high.

Table 8 lists the OC radar cross-section, σ_{OC} . The mean measured OC cross-section (both Arecibo and Goldstone data) for Mithra is $\sigma_{\text{OC}} = 0.42 \pm 0.17$ km². The OC radar albedo is calculated by dividing the measured OC cross-section by the projected area of the model. We obtain consistent OC radar albedos of

Table 7

Close approaches for Mithra based on the orbital solution #68.

Date (coordinate time)	Body	CAdist (AU)	MINdist (AU)	MAXdist (AU)	Vrel (km s ⁻¹)	TCA3Sg (min)
A.D. 1602 August 10.42424	Earth	0.096603	0.096145	0.097063	19.783	45.72
A.D. 1615 August 09.67753	Earth	0.089114	0.080460	0.097952	19.428	922.38
A.D. 1628 August 09.49165	Earth	0.085290	0.074560	0.096383	19.473	1176.10
A.D. 1651 April 17.10156	Venus	0.029173	0.029033	0.029313	9.256	593.82
A.D. 1664 January 06.34485	Mars	0.095954	0.092705	0.099203	18.622	294.69
A.D. 1664 March 10.60422	Earth	0.075274	0.072109	0.078562	18.857	431.75
A.D. 1697 February 13.28837	Mars	0.032422	0.032134	0.032808	17.047	139.59
A.D. 1706 August 31.41195	Venus	0.031066	0.031001	0.031131	9.230	157.98
A.D. 1729 August 10.62671	Earth	0.061932	0.061430	0.062436	18.598	69.51
A.D. 1762 January 22.54108	Venus	0.045713	0.045377	0.046047	10.788	120.87
A.D. 1765 March 12.28086	Earth	0.093986	0.093553	0.094420	19.581	46.61
A.D. 1781 January 07.64429	Vesta	0.073318	0.073081	0.073555	11.874	15.41
A.D. 1794 August 31.63016	Venus	0.037587	0.037420	0.037754	10.795	66.47
A.D. 1827 March 21.97209	Earth	0.059563	0.059214	0.059919	16.508	94.08
A.D. 1846 May 10.65532	Vesta	0.090676	0.089687	0.091667	12.047	80.09
A.D. 1846 December 21.01411	Venus	0.063721	0.062036	0.065400	11.766	404.90
A.D. 1853 August 11.44425	Earth	0.052501	0.052014	0.052998	17.998	94.68
A.D. 1856 October 03.73940	Venus	0.032347	0.032153	0.032541	9.597	167.55
A.D. 1856 December 28.50540	Mars	0.079120	0.078714	0.079526	15.795	35.55
A.D. 1879 January 15.13059	Vesta	0.047588	0.047545	0.047631	11.181	3.86
A.D. 1909 January 16.03817	Venus	0.040111	0.039841	0.040380	10.187	127.48
A.D. 1912 March 18.74426	Earth	0.071580	0.071278	0.071884	18.589	43.27
A.D. 1919 January 31.62547	Mars	0.040440	0.040252	0.040632	17.518	27.82
A.D. 1944 May 17.54748	Vesta	0.030770	0.030745	0.030795	11.294	4.05
A.D. 1951 July 09.48218	Venus	0.028461	0.028459	0.028462	9.278	12.38
A.D. 1977 January 14.62488	Vesta	0.029472	0.029468	0.029476	11.507	0.79
A.D. 1993 December 23.05494	Venus	0.018640	0.018640	0.018641	9.771	0.72
A.D. 2000 August 14.34276	Earth	0.046542	0.046542	0.046542	17.571	0.00
A.D. 2009 September 17.98843	Vesta	0.034266	0.034264	0.034267	11.269	0.12
A.D. 2056 February 04.08307	Venus	0.016640	0.016638	0.016641	9.852	2.46
A.D. 2059 January 20.81068	Mars	0.096285	0.096271	0.096298	15.841	1.33
A.D. 2098 August 09.79261	Venus	0.092416	0.092319	0.092514	13.705	15.02
A.D. 2108 May 08.35213	Venus	0.066347	0.066330	0.066365	12.674	3.47
A.D. 2134 August 18.65724	Earth	0.052931	0.052813	0.053050	17.943	26.47
A.D. 2150 November 04.67652	Venus	0.013836	0.013784	0.013888	9.825	205.68
A.D. 2203 February 06.63767	Venus	0.057081	0.054539	0.059608	11.995	586.32
A.D. 2229 June 13.52853	Mars	0.070934	0.049113	0.095666	18.123	2081.80
A.D. 2235 October 15.83885	Venus	0.052897	0.022275	0.081507	11.571	7993.70
A.D. 2245 April 02.11114	Mars	0.038825	0.036647	0.041069	17.696	342.63
A.D. 2255 March 31.24666	Earth	0.051588	0.050147	0.076379	16.942	5211.60

Mithra encounters with Earth, Venus, Mars, Ceres, Pallas, and Vesta, less than 0.1 AU, limited in time by Earth encounters for which the 3- σ Earth time-of-encounter uncertainty is less than 10 days and the 3- σ Earth encounter distance uncertainty is less than 0.1 AU. These criteria are satisfied over the interval 1602–2255, defining the approximate limits of reliable Earth encounter prediction for Mithra. The encounter observed by radar in 2000 was the closest for the foreseeable future. Nominal close-approach dates are given. CAdist is the nominal close-approach distance at the nominal close-approach time, uncorrected for light travel time. MINdist and MAXdist are the encounter distance 3- σ uncertainties at the nominal encounter time. Vrel is the nominal relative velocity. TCA3Sg is close-approach time 3- σ uncertainty. Integrations were performed using the DE405 planetary ephemeris to include relativistic point-mass perturbations due to the Sun, Planets, and Moon, as well as Ceres, Pallas, and Vesta. The limits of predictability for km-sized and smaller objects having multiple planetary encounters over centuries can be affected by additional factors such as radiation pressure, Yarkovsky acceleration, planetary mass uncertainties, and asteroid perturbations. These factors are not included here, since the relevant physical models are imprecisely defined and key parameters are unmeasured.

$\eta_{OC} = 0.17 \pm 0.04$ for the prograde model and $\eta_{OC} = 0.16 \pm 0.04$ for the retrograde model. These are close to the average value for NEAs ($\eta_{OC} = 0.17 \pm 0.11$, $N = 28$, http://echo.jpl.nasa.gov/~lance/asteroid_radar_properties/nea.radaralbedo.html).

We used our OC cross-section and the “Eros-calibrated” approach from Magri et al. (2001) to estimate the near-surface solid density. In order to establish a maximum value we assumed a porosity $p = 0$. For the prograde model, we obtain a maximum near-surface solid density of 3.0 g cm^{-3} and a maximum density of 2.9 g cm^{-3} for the retrograde model. The uncertainty of these values is at least a few tens of percent due to assumptions made for the analysis (Magri et al., 2001).

6. Mithra's gravitational/dynamical environment

6.1. Mithra's surface environment

Given Mithra's shape and spin state, we can evaluate the surface environment on this asteroid (Scheeres et al., 1996). Of most inter-

est is the gravitational slope distribution across the body, as this places implicit constraints on the strength of the surface. The gravitational slope is the angle that a plumb line would make with the normal to the surface. Specifically, if regions have slopes above 35–40°, we infer that the surface has some degree of cohesiveness and tensile strength (Holsapple, 2001, 2004). For a slowly rotating body such as Mithra, the slope is dominated by the total gravitational attraction and surface topography. For a homogeneous density, the surface slopes are independent of interior density.

Due to the mirror-symmetries between the retrograde and direct shape models, the slope statistics and distributions are similar between the two bodies. We assumed a bulk density of 2 g cm^{-3} . In Fig. 8, we present the slope distributions for the observed hemispheres of the asteroid (northern for the prograde model, southern for the retrograde model). Across both models we find slopes that range from zero to nearly 60°. Slopes of 60° exceed the angle of repose and suggest bare rock (i.e. no regolith). We note that Asteroid 25143 Itokawa also has local slope regions up to 60°, most notably along the “face” of the “head” (Demura et al., 2006). These regions are very rough, with many large boulders exposed.

Table 8

Disk-integrated properties.

Arecibo and Goldstone CW data					
Date	Obs.	σ_{OC} (km ²)	SC/OC	# Looks	
2000 July 22	A	0.44	0.33 ± 0.01	48	
2000 July 23	A	0.60	0.13 ± 0.02	45	
2000 July 25	A	0.55	0.21 ± 0.02	82	
2000 July 28	A	0.35	0.39 ± 0.02	35	
2000 August 06	G	0.18	0.48 ± 0.01	77	
		0.42 ± 0.17	0.31 ± 0.14		
Prograde model					
Date	Long (°)	Lat (°)	ψ (°)	Area (km ²)	η_{OC}
2000 July 22	109	75	251	2.91	0.15
2000 July 23	342	76	18	2.83	0.21
2000 July 25	88	77	272	2.90	0.19
2000 July 28	63	79	297	2.89	0.12
					0.17 ± 0.04
Retrograde model					
Date	Long (°)	Lat (°)	ψ (°)	Area (km ²)	η_{OC}
2000 July 22	122	−75	238	3.16	0.14
2000 July 23	354	−76	6	3.05	0.20
2000 July 25	99	−77	261	3.14	0.18
2000 July 28	73	−80	287	3.11	0.11
					0.16 ± 0.04

Top: disk-integrated OC cross-section (σ_{OC}), circular polarization ratio (SC/OC) estimated from Arecibo and Goldstone CW spectra. Arecibo CW data were reduced with 0.2 Hz resolution for all but the July 22 data, which have a resolution of 0.03 Hz. The resolution was chosen in order to get enough looks to obtain Gaussian noise statistics. The number of looks represents the number of statistically independent measurements that were used to get the average SC and OC spectra. In the second and third part of this table we list each model's predictions for the projected surface area at the mid-receive epoch. Lat, Long, and ψ represent model estimates of the subradar latitude and longitude, as well as the rotation phase at the time when CW spectra were obtained. OC radar albedo (η_{OC}) is calculated by dividing the cross-section (σ_{OC}) by the projected area.

The gravitational potential also varies strongly across the surfaces of both models of Mithra (see Fig. 9). We find that the deepest portion of the gravitational potential lies at the contact region between the two bodies. By analogy with Itokawa, we suggest that the regions of deepest gravitational potential may contain accumulated loose material and low slope. We note that the deepest locations for both models also correspond to low slopes.

6.2. Mithra's spin state evolution

The spin states of moderately sized asteroids (<10 km) are strongly affected by collisions between asteroids, by close plane-

tary encounters, and by the thermal torque originating from absorption and re-emission of solar radiation from an asteroid's surface. The theory of the YORP (Yarkovsky–O'Keefe–Radzievskii–Paddack) effect (Rubincam, 2000) describes the evolution of spin state and obliquity due to solar radiation. We apply the theory outlined in Scheeres (2007a) and Scheeres and Mirrahimi (2008) to our shape model of Mithra. The detailed topography of the unobserved regions is important for the overall YORP evolution (Statler, 2009), so in the absence of any other information, we adopt the models at face value and explore their implications. We note that a small change in shape or small center-of-mass offset can completely reverse the torque direction, thus estimated spin acceleration, and should be taken as only dimensional estimates.

Due to the near mirror-symmetries between the models the YORP responses of both bodies are quite similar. Assuming a density of 2 g cm^{-3} , we compute current YORP rotational accelerations of approximately $4.5 \times 10^{-11} \text{ rad s}^{-1} \text{ year}^{-1}$ for the prograde model and $4.2 \times 10^{-11} \text{ rad s}^{-1} \text{ year}^{-1}$ for the retrograde model, leading to doubling of the spin rate in approximately 575,000 and 615,000 years, respectively, comparable to that observed for Asteroid (54509) YORP (Taylor et al., 2007). This is also the time it would take Mithra to spin up to its current spin rate from no rotation, assuming we apply the current, constant spin acceleration to the body.

We find that both models have obliquities that should be moving away from 90° . They are currently at $+68^\circ$ and $+106^\circ$ with respect to Mithra's orbital plane. More precise estimates of the current obliquity rate require an estimate of the body's thermal inertia, which we do not know. However, both models indicate that Mithra's obliquity was closer to 90° in the past. Using the terminology for the dynamical evolution of the asteroid's spin state presented in Scheeres and Mirrahimi (2008), we classify Mithra to be a Type II+, meaning that its asymptotic spin state in the future is a slow rotation with obliquity going towards 0° or 180° . Its asymptotic spin state in the past is a slow rotation with obliquity approaching 90° .

We made a preliminary estimate (at nominal values of the obliquities) of the relationship between Mithra's pole precession frequency α (Laskar and Robutel, 1993; Laskar et al., 1993; Skoglöv et al., 1996) and the nodal precession frequency $d\Omega/dt$. The prograde model has $\alpha = 400'' \text{ year}^{-1}$ while the retrograde model has $\alpha = -296'' \text{ year}^{-1}$. We have numerically integrated Mithra's node angle from year 1600 to year 2200, and based on this, we established a linear downward secular trend with a slope of $-31'' \text{ year}^{-1}$. We conclude that since the pole precesses rapidly compared to the nodal precession rate the obliquity precesses at a more or less constant angle around the orbit normal.

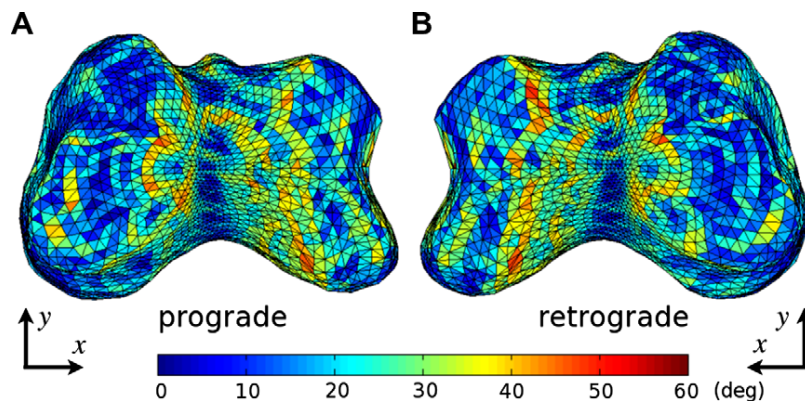


Fig. 8. Gravitational slopes for the prograde (A) and retrograde (B) models. We only show the side of Mithra (north or south pole view) that was observed by radar.

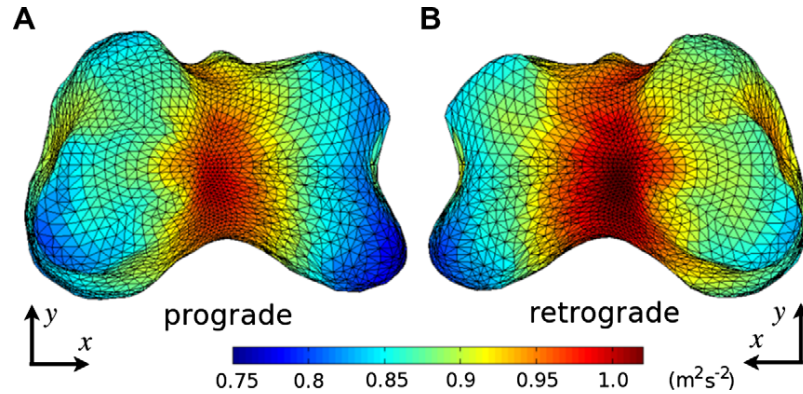


Fig. 9. Gravitational potential for the prograde (A) and retrograde (B) models. We only show the side of Mithra that was observed by radar.

7. Discussion

7.1. Abundance of contact binaries in the NEA population

Radar observations suggest that candidate contact binaries make up about 10% of the NEAs larger than 200 m in diameter (Benner et al., 2006). Mithra's bifurcated shape clearly establishes that it is a candidate contact binary, which we define as "an asteroid consisting of two lobes that are in contact, have a bimodal mass distribution, and might have once been separate" (Benner et al., 2006). We are confident that Mithra's lobes are in compressive contact not only due to the visible bridge, but also because a true binary configuration with an orbital period of 67 h would imply an implausibly low bulk density. Table 9 lists all known candidates in the radar sample, which now includes 20 objects. When combined with the NEA binary systems population (~16%) with the same size threshold (Margot et al., 2002; Pravec et al., 2006) this indicates that at least 25% of the NEAs are contact binaries or true binary systems.

Table 9 shows that candidate contact binaries appear to be a very diverse group with a wide range of sizes and rotational periods. We do not include 25143 Itokawa (Demura et al., 2006; Fujiwara et al., 2006; Scheeres, 2007b) or Toutatis (Hudson and Ostro, 1995) because they do not have a bimodal mass distribution. Castalia (Hudson and Ostro, 1994) and 2063 Bacchus (Benner et al., 1999) are the only other contact binaries for which we have a model, although the model for Mithra is much more detailed.

7.2. Origin of Mithra's shape

How did Mithra's shape originate? Mithra's bimodal mass distribution may be a product of a low-velocity collision, perhaps between the components of a true binary system (Farinella, 1992; Hudson and Ostro, 1995; Chauvineau et al., 1995; Bottke and Melosh, 1996a,b; Leinhardt et al., 2000; Taylor, 2009). Leinhardt et al. (2000) presented a modeling study where they simulated slow collisions between two 1-km diameter rubble piles and found that low-speed ($<10 \text{ m s}^{-1}$), off-center collisions could produce peanut-

Table 9

Candidate contact binaries observed by radar.

Asteroid	Diameter (km)	Res'n (m)	Period (h)	Radar references
4769 Castalia	1.0	300.0	4.0	Ostro et al. (1990) and Hudson and Ostro (1994)
68346 2001 KZ66	1.0	15.0	~6.0	Nolan et al. (unpublished)
2005 CR37	1.0	15.0	6.5	Benner et al. (2006)
*2007 VD12	0.5	19.0	7.4 ^a	Benner et al. (unpublished)
11066 Sigurd	3.0	75.0	8.5	Benner et al. (2004)
*1996 HW1	2.0	75.0	8.8 ^b	Nolan et al. (unpublished)
*179806 2002 TD66	0.3	7.5	9.5 ^c	Nolan et al. (unpublished)
*2000 YF29	0.5	15.0	<12.0	Benner et al. (unpublished)
*2002 HK12	0.6	15.0	12.7 ^b	Nolan et al. (unpublished)
2063 Bacchus	0.6	75.0	15.1	Benner et al. (1999)
*1998 FW4	0.4	7.5	~18.0	Busch et al. (unpublished)
2002 NY40	0.4	7.5	20.0 ^d	Nolan et al. (unpublished)
*2004 XL14	0.4	7.5	~1 day	Brozovic et al. (unpublished)
52387 1993 OM7	1.0	15.0	>26.0 ^b	Ostro et al. (unpublished)
*2008 SV11	~0.8	15.0	32.4 ^c	Nolan et al. (unpublished)
*2007 TU24	0.3	7.5	1–2 days	Ostro et al. (unpublished)
*4450 Pan	1.0	15.0	2–3 ^{a,b} days	Nolan et al. (unpublished)
4486 Mithra	1.6	19.0	67.4	This paper
2002 FC	0.7	15.0	Days	Ostro et al. (unpublished)
2004 RF84	2.4	15.0	Weeks	Benner et al. (unpublished)

Candidate contact binaries sorted by rotation period. Asteroids marked with an asterisk have been observed for the first time since the first version of this table was published in Benner et al. (2006). 2001 KZ66 has a corrected rotation period of ~6.0 h as opposed to the originally reported 2.7 h. We list each object's diameter, radar imaging resolution in range, and rotation period. Unless superscripted by a letter (photometry reference), the periods have been estimated (sometimes very roughly) from sequences of radar images only.

^a Carbognani (2008).

^b Pravec et al. (unpublished) – <http://www.asu.cas.cz/~ppravec/newres.txt>.

^c Warner et al. (unpublished) – <http://www.minorplanetobserver.com/>.

^d Pravec et al. (2005).

shaped contact binaries. Alternatively, Mithra's shape may be a result of distortion of a gravitationally-bound agglomerate that occurred during close approaches to a planet (Asphaug and Benz, 1996; Richardson et al., 1998, 2002; Merline et al., 2002; Bottke et al., 2002; Richardson and Walsh, 2006). Spin-up due to YORP or a close planetary encounter may eventually lead Mithra to become a true binary.

7.3. Mithra's despinning time does not require an NPA spin state

With period of 67.5 h, Mithra is clearly a slow rotator. Among ~450 NEAs with known rotation periods (<http://www.asu.cas.cz/~ppravec/newres.txt>), only ~8% rotate more slowly than Mithra. Pravec et al. (2005) suggested that YORP is the most likely explanation for slow rotation, although planetary encounters could also slow the rotation. There have been many recent theoretical papers on the influence of YORP and of planetary flybys on asteroid spin states (Bottke et al., 2002; Scheeres et al., 2004; Scheeres, 2007a,b; Scheeres and Mirrahimi, 2008).

Many slow rotators are NPA rotators, and an additional hint that a slow rotator may be an NPA rotator is the damping timescale τ . This represents the timescale in which NPA rotators dissipate energy and evolve toward PA rotation (Burns and Safronov, 1973). Harris (1994) expressed the damping timescale $\tau = P^3/(C^3 D^2)$, where P is the asteroid's rotation period in hours, D is the mean diameter in km, and all other factors (bulk density, rigidity, shape, quality factor) are lumped into a constant C , which has a value (within a factor of 2.5) of 17. Pravec and Harris (2000) suggested "that tumbling rotation is the norm for slowly rotating asteroids where the damping time scale is long" and Pravec et al. (2005) presented evidence that most asteroids larger than ~0.4 km with estimated damping timescales of 4.5 byr and longer are NPA rotators. We define τ_{norm} as the damping timescale τ normalized to 4.5 byr. Asteroids with $\log \tau_{\text{norm}}$ values just a few tenths less than zero are in the region where the PA rotation starts dominating. For Mithra, $\log \tau_{\text{norm}} = 0.69$ which is in the region where Pravec et al. (2005) predominantly find NPA rotators. However, our results showed that if an NPA component exists in Mithra's rotation, it is very small. In fact, Pravec et al. (2005) found several PA rotators in the τ_{norm} region dominated by tumblers (e.g. (3102) Krok, with $\tau_{\text{norm}} = 1.8$), which implies that the damping timescale value is only an approximate criterion. An alternative implication for the damping timescale is that slow rotation per se does not lead to tumbling, that is, the mechanism of slowing (YORP) is not the same as the mechanism exciting NPA rotation. In order for a slow rotator to become an NPA rotator, something other than despinning has to trigger NPA rotation.

7.4. Future observation opportunities and objectives

The next opportunity to observe Mithra with radar at SNRs comparable to those discussed here will occur in April 2059. However, Mithra will be a good target for lightcurve measurements in March 2010 when it approaches within 0.19 AU, reaches a solar elongation of 127°, and becomes brighter than magnitude 15. The prograde pole estimates suggest that the lightcurves will sample latitudes from +50° to −50° between February 10 and March 20. The equatorial aspect occurs in early-to-mid March and coincides with large solar phase angles when the lightcurve amplitude is likely to exceed a full magnitude. Photometric observations in 2010 could significantly refine the spin state and potentially elucidate whether Mithra is a non-principal axis rotator. Additionally, this would help to constrain the shape on the side unseen by radar. Thermal IR observations could constrain the thermal inertia and thus improve our predictions for Mithra's spin evolution due to YORP. Our optical albedo and SC/OC ratio hint that Mithra could

be an S-class object, but only spectroscopy will be able to determine Mithra's taxonomic class with higher certainty.

Acknowledgments

We dedicate this paper to the memory of Steve Ostro who passed away as we were finalizing this analysis. Mithra fascinated him since the time he observed it in 2000 and he continued to be involved in this study until the very end. Steve was the most amazing mentor, colleague, and friend.

We would like to thank Alan W. Harris (USA) and Patrick A. Taylor for insightful reviews that improved the paper. We thank the Arecibo and Goldstone technical and support staffs for help with the radar observations. The Arecibo Observatory is part of the National Astronomy and Ionosphere Center, which is operated by Cornell University under a cooperative agreement with the National Science Foundation (NSF) and, at the time of this experiment, also had support from the National Aeronautics and Space Administration (NASA). Some of this work was performed at the Jet Propulsion Laboratory, California Institute of Technology, under contract with NASA. This material is based in part upon work supported by NASA under the Science Mission Directorate Research and Analysis Programs.

Appendix A. Supplementary material

Supplementary data associated with this article can be found, in the online version, at doi:10.1016/j.icarus.2010.01.035.

References

- Asphaug, E., Benz, W., 1996. Size, density, and structure of Comet Shoemaker-Levy 9 inferred from the physics of tidal breakup. *Icarus* 121, 225–248.
- Benner, L.A.M., and 11 colleagues, 1999. Radar observations of Asteroid 2063 Bacchus. *Icarus* 139, 309–327.
- Benner, L.A.M., Ostro, S.J., Hudson, R.S., Rosema, K.D., Jurgens, R.F., Yeomans, D.K., Campbell, D.B., Chandler, J.F., Shapiro, I.I., 2002. Radar observations of Asteroid 3908 Nyx. *Icarus* 158, 379–388.
- Benner, L.A.M., Nolan, M.C., Carter, L.M., Ostro, S.J., Giorgini, J.D., Magri, C., Margot, J.-L., 2004. Radar imaging of near-Earth Asteroid 11066 Sigurd. *Bull. Am. Astron. Soc.* 36, 1143.
- Benner, L.A.M., Nolan, M.C., Ostro, S.J., Giorgini, J.D., Pray, D.P., Harris, A.W., Magri, C., Margot, J.-L., 2006. Near-Earth Asteroid 2005 CR37: Radar images and photometry of a candidate contact binary. *Icarus* 182, 474–481.
- Benner, L.A.M., and 10 colleagues, 2008. Near-Earth asteroid surface roughness depends on compositional class. *Icarus* 198, 294–304.
- Bottke, W.F., Melosh, H.J., 1996a. Formation of the asteroid satellites and doublet craters by planetary tidal forces. *Nature* 381, 51–53.
- Bottke, W.F., Melosh, H.J., 1996b. Binary asteroids and the formation of doublet craters. *Icarus* 124, 372–391.
- Bottke, W.F., Vokrouhlicky, D., Rubincam, D.P., Broz, M., 2002. The effect of Yarkovsky thermal forces on the dynamical evolution of asteroids and meteoroids. In: Bottke, W.F., Cellino, A., Paolicchi, P., Binzel, R.P. (Eds.), *Asteroids III*. University of Arizona Press, Tucson, pp. 395–408.
- Burns, J.A., Safronov, V.S., 1973. Asteroid nutation angles. *Mon. Not. R. Astron. Soc.* 165, 403–411.
- Campins, H., Rieke, G.H., Lebofsky, M.J., 1985. Absolute calibration of photometry at 1 through 5 microns. *Astron. J.* 90, 896–899.
- Carbognani, A., 2008. Lightcurve photometry of NEAs 4450 Pan, (170891) 2004 TY16, 2002 RC118, and 2007 VD12. *Minor Planet Bull.* 35, 109–110.
- Chauvineau, B., Farinella, P., Harris, A.W., 1995. The evolution of Earth-approaching binary asteroids: A Monte Carlo dynamical model. *Icarus* 115, 36–46.
- Demura, H., and 19 colleagues, 2006. Pole and global shape of 25143 Itokawa. *Science* 312, 1347–1349.
- Farinella, P., 1992. Evolution of Earth-crossing binary asteroids due to gravitational encounters with the Earth. *Icarus* 96, 284–285.
- Fujiwara, A., and 21 colleagues, 2006. The rubble-pile asteroid Itokawa as observed by Hayabusa. *Science* 312, 1330–1334.
- Harris, A.W., 1994. Tumbling asteroids. *Icarus* 107, 209–211.
- Holsapple, K.A., 2001. Equilibrium configurations of solid cohesionless bodies. *Icarus* 154, 432–448.
- Holsapple, K.A., 2004. Equilibrium figures of spinning bodies with self-gravity. *Icarus* 172, 272–303.
- Hudson, S., 1993. Three-dimensional reconstruction of asteroids from radar observations. *Remote Sens. Rev.* 8, 195–203.

- Hudson, R.S., Ostro, S.J., 1994. Shape of Asteroid 4769 Castalia (1989 PB) from inversion of radar images. *Science* 263, 940–943.
- Hudson, R.S., Ostro, S.J., 1995. Shape and non-principal axis spin state of Asteroid 4179 Toutatis. *Science* 270, 84–86.
- Hudson, R.S., Ostro, S.J., 1999. Physical model of Asteroid 1620 Geographos from radar and optical data. *Icarus* 140, 369–378.
- Hudson, R.S., Ostro, S.J., Harris, A.W., 1997. Constraints on spin state and Hapke parameters of Asteroid 4769 Castalia using lightcurves and a radar-derived shape model. *Icarus* 130, 165–176.
- Laskar, J., Robutel, P., 1993. The chaotic obliquity of the planets. *Nature* 361, 608–612.
- Laskar, J., Joutel, F., Robutel, P., 1993. Stabilization of the Earth's obliquity by the Moon. *Nature* 361, 615–617.
- Leinhardt, Z.M., Richardson, D.C., Quinn, T., 2000. Direct N-body simulations of rubble pile collisions. *Icarus* 146, 133–151.
- Magri, C., Consolmagno, G.J., Ostro, S.J., Benner, L.A.M., Beeny, B.R., 2001. Radar constraints on asteroid regolith properties using 433 Eros as ground truth. *Meteorit. Planet. Sci.* 36, 1697–1709.
- Magri, C., Ostro, S.J., Scheeres, D.J., Nolan, M.C., Giorgini, J.D., Benner, L.A.M., Margot, J.-L., 2007. Radar observations and a physical model of Asteroid 1580 Betulia. *Icarus* 186, 152–177.
- Margot, J.L., Nolan, M.C., Benner, L.A.M., Ostro, S.J., Jurgens, R.F., Giorgini, J.D., Slade, M.A., Campbell, D.B., 2002. Binary asteroids in the near-Earth object population. *Science* 296, 1445–1448.
- Merline, W.J., Weidenschilling, S.J., Durda, D.D., Margot, J.-L., Pravec, P., Storrs, A.D., 2002. Asteroids do have satellites. In: Bottke, W.F., Cellino, A., Paolicchi, P., Binzel, R.P. (Eds.), *Asteroids III*. University of Arizona Press, Tucson, pp. 289–312.
- Michel, P., Froeschlé, Ch., Farinella, P., 1996. Dynamical evolution of two near-Earth asteroids to be explored by spacecraft. *Astron. Astrophys.* 313, 993–1007.
- Ostro, S.J., 1993. Planetary radar astronomy. *Rev. Mod. Phys.* 65, 1235–1279.
- Ostro, S.J., Chandler, J.F., Hine, A.A., Rosema, K.D., Shapiro, I.I., Yeomans, D.K., 1990. Radar images of Asteroid 1989 PB. *Science* 248, 1523–1528.
- Ostro, S.J., Hudson, R.S., Benner, L.A.M., Nolan, M.C., Margot, J.-L., Giorgini, J.D., Jurgens, R.F., Rose, R., Yeomans, D.K., 2000. Radar observations of Asteroid 4486 Mithra. *Bull. Am. Astron. Soc.* 32, 1003.
- Ostro, S.J., and 15 colleagues, 2004. Radar observations of Asteroid 25143 Itokawa (1998 SF36). *Meteorit. Planet. Sci.* 39, 407–424.
- Ostro, S.J., and 12 colleagues, 2005. Radar observations of Itokawa in 2004 and improved shape estimation. *Meteorit. Planet. Sci.* 40, 1563–1574.
- Pravec, P., Harris, A.W., 2000. Fast and slow rotation of asteroids. *Icarus* 148, 12–20.
- Pravec, P., Harris, A.W., 2007. Binary asteroid population. I. Angular momentum content. *Icarus* 190, 250–259.
- Pravec, P., and 19 colleagues, 2005. Tumbling asteroids. *Icarus* 173, 108–131.
- Pravec, P., and 56 colleagues, 2006. Photometric survey of binary near-Earth asteroids. *Icarus* 181, 63–93.
- Richardson, D.C., Walsh, K.J., 2006. Binary minor planets. *Annu. Rev. Earth Planet. Sci.* 34, 47–81.
- Richardson, D.C., Bottke, W.F., Love, S.G., 1998. Tidal distortion and disruption of Earth-crossing asteroids. *Icarus* 134, 47–76.
- Richardson, D.C., Leinhardt, Z.M., Melosh, H.J., Bottke, W.F., Asphaug, E., 2002. Gravitational aggregates: Evidence and evolution. In: Bottke, W.F., Cellino, A., Paolicchi, P., Binzel, R.P. (Eds.), *Asteroids III*. University of Arizona Press, Tucson, pp. 501–515.
- Rubincam, D.P., 2000. Radiative spin-up and spin-down of small asteroids. *Icarus* 148, 2–11.
- Scheeres, D.J., 2007a. The dynamical evolution of uniformly rotating asteroids subject to YORP. *Icarus* 188, 430–450.
- Scheeres, D.J., 2007b. Rotational fission of contact binary asteroids. *Icarus* 189, 370–385.
- Scheeres, D.J., Mirrahimi, S., 2008. Rotational dynamics of a Solar System body under solar radiation torques. *Celest. Mech. Dynam. Astron.* 101, 69–103.
- Scheeres, D.J., Ostro, S.J., Hudson, R.S., Werner, R.A., 1996. Orbits close to Asteroid 4769 Castalia. *Icarus* 121, 67–87.
- Scheeres, D.J., Marzari, F., Rossi, A., 2004. Evolution of NEO rotation rates due to close encounters with Earth and Venus. *Icarus* 170, 312–323.
- Skoglöv, E., Magnusson, P., Dahlgren, M., 1996. Evolution of the obliquities for ten asteroids. *Planet. Space Sci.* 44, 1177–1183.
- Statler, T.S., 2009. Extreme sensitivity of the YORP effect to small-scale topography. *Icarus* 202, 502–513.
- Taylor, P.A., 2009. Preferential production of contact binary asteroids with components of similar mass via angular momentum loss. *Bull. Am. Astron. Soc.* 41, 905.
- Taylor, P.A., and 11 colleagues, 2007. Spin rate of Asteroid (54509) 2000 PH5 increasing due to the YORP effect. *Science* 316, 274–277.